Dual-Polarized Probe for Planar Near-Field Measurement

Sabin Kumar Karki, Juha Ala-Laurinaho, and Ville Viikari, *Senior Member, IEEE*

***Abstract*—A dual-polarized probe enables the simultaneous sampling of two orthogonal polarizations, which decreases the time for the characterization of co- and cross-polar properties of the antenna under test in transmission mode by 50%. In this work, a dual-polarized probe comprising of a square waveguide and grating polarizer-based orthomode transducer is presented. The Ku-band dual-polarized probe is manufactured in-house using additive manufacturing and coated with conductive paint. The simulated and measured −10 dB impedance bandwidth is between 10.7 and 14.5 GHz. The peak simulated and measured coupling between the orthogonal polarizations is less than −60 dB and −40 dB, respectively.**

***Index Terms*—3-D printing, conductive paint, dual-polarized, near-field, orthomode transducer, probe, square waveguide.**

I. Introduction

THE near-field (NF) measurement technique is used to characterize the radiation properties of an antenna. In the NF measurement, the probe antenna samples the radiating NF of an antenna under test (AUT). The field sampled in uniform grid on a planar, cylindrical, or spherical surface is then transformed into the far-field [1]. An AUT needs to be characterized for both co- and cross-polar properties. Typically, a NF-probe antenna supports single polarization and the measurement is done twice by rotating the probe 90° to obtain both the co- and cross-polarized response, which doubles the measurement time. A dual-polarized probe (DPP), a single antenna that supports two orthogonal polarizations, together with a dual-channel receiver can halve the data acquisition time of the co- and cross-polar measurements of the AUT in the transmission mode. For a DPP, high isolation and axial ratio between the orthogonal linear polarizations are essential for accurate characterization of the AUT [2]. In addition, the receiver channels' responses, amplitude and phase, of both the polarizations should be balanced.

A rectangular open-ended waveguide (OEWG) is generally used as the probe antenna in a planar NF measurement [3]. A rectangular OEWG is linearly polarized and it is mechanically rotated by 90° for cross-polar measurement of an AUT. The mechanical rotation and double scanning can be avoided with two closely placed orthogonally polarized probes, which gives high isolation [4]. However, the closely positioned orthogonal probes distort each other's radiation pattern.

A DPP is a combination of an orthomode transducer (OMT) and a radiating element [5]. The OMTs are used to generate or receive the orthogonally polarized waves [6]. A simple method to implement dual-polarization is to use a square waveguide with a coaxial connections on the adjacent walls [7]. Since both the coaxial connections are at the same distance from the shorting wall and close to each other, the coupling between the orthogonal feed ports is high, approx. −15 dB. The quad-ridge waveguide with the coaxial feeds from the orthogonal directions achieved the broadband impedance matching [8]. As the orthogonal feeds are slightly offset along the waveguide axis, the isolation improves slightly to approx. −25 dB. In [9], the DPP is implemented with inverted quad-ridge and differential feed. The design achieved the reflection coefficient $|S_{11}| < -12$ dB, and coupling $|S_{21}|$ between two polarization is less than −55 dB in the frequency bandwidth of 4:1. The differential feed requires four feeds for two orthogonal polarizations, one 180° phase shifted feed for each polarization. The phase imbalance between the differential feed branch can increase the reflection significantly [9]. The differential feeding is implemented using additional beamforming network or power division network [5].

The OMTs based on a power division network and differential feeding of the turnstile and Bøifot junctions are used in radio-astronomy receivers. The turnstile-junction-based OMT proposed in [10] achieved $|S_{11}| < -20$ dB, and $|S_{21}| < -50$ dB, for more than 50% bandwidth [11]. The turnstile OMT based probe antennas have been used in spherical NF measurement [12], [13]. The OMT based on Bøifot junction can also provide high isolation and wide-band operation [14], [15]. The turnstile and Bøifot junctions require four and three subarms/branches, respectively, to receive or transmit two orthogonal polarizations with high isolation. The implementation of both the turnstile and Bøifot based OMT requires larger volume due to division of single feed into two subarms.

In this letter, a square-waveguide DPP based on a novel grating-polarizer OMT is proposed. The proposed design is simple, has a small form factor, requires only one feed per polarization, and the coupling between the orthogonal polarizations, under ideal conditions, is better than that of most of the state-of-art solutions. The article introduces the OMT design and studies the effects of the polarizer dimensions and its location with the full-wave simulation. A Ku-band DPP is designed to achieve high isolation between orthogonal polarizations. The

Manuscript received 24 July 2022; accepted 10 September 2022. Date of publication 1 November 2022; date of current version 3 March 2023. This work was supported by Business Finland through RF Sampo Project. *(Corresponding author: Sabin Kumar Karki.)*

The authors are with the Department of Electronics and Nanoengineering, Aalto University, FI-0076 Espoo, Finland (e-mail: sabin.karki@aalto.fi; juha.ala-laurinaho@aalto.fi; ville.viikari@aalto.fi).

Digital Object Identifier 10.1109/LAWP.2022.3218731

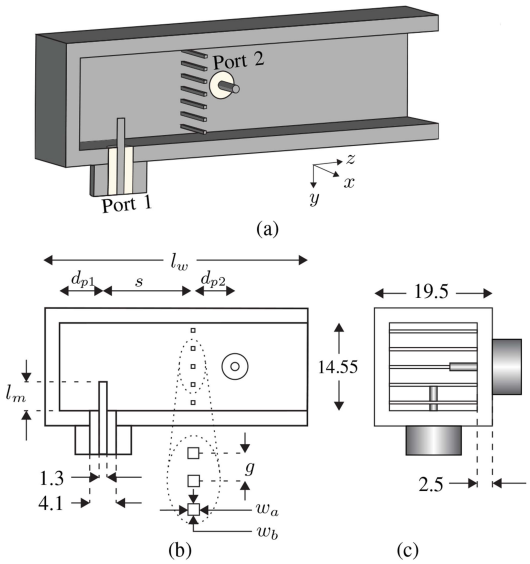

Fig. 1. (a) Cut-away view, (b) side view, and (c) front view of the proposed OMT. Dimensions are in mm.

prototype is fabricated in-house using additive manufacturing and conductive paint. The simulation and measurement results are compared to examine the applicability of the proposed design.

II. Orthomode Transducer

This section presents the design and parametric study of the OMT. A square waveguide, 14.55 mm wide, is selected to operate at Ku-band. The cutoff frequency of the TE_{10} mode of the square waveguide is 10.3 GHz, whereas the cutoff frequency of the first higher order mode (TE_{11}) is 14.6 GHz. Hence, the operation bandwidth of the OMT is primarily limited by the bandwidth of the square waveguide.

The square waveguide is fed using coaxial connectors [16]. The length of the coaxial inner conductor in the waveguide l_m is 4.5 mm. The coaxial feeds for the orthogonal linear polarizations are placed on the adjacent walls of the square waveguide as shown in Fig. 1. When both the coaxial feeds are at the same distance from the shorting wall, $d_{p1} = 8.6$ mm, and the grating polarizer is not used, the desired impedance bandwidth for both the ports can be achieved, i.e., reflection coefficient of Port 1 $|S_{11}|$ and Port 2 $|S_{22}|$ is below -10 dB. However, the coupling between Ports 1 and 2 $|S_{21}|$ is higher, approx. -15 dB. The coupling between the orthogonal polarizations can be minimized by displacing one port, i.e., Port 2, along the waveguide axis, i.e., z-axis, away from the shorting wall. When Port 2 moves away, $|S_{11}|$ is mostly unaffected and $|S_{22}|$ is higher and the impedance bandwidth becomes narrower because the field reflected from the shorting wall does not add constructively in the entire frequency range as d_{p2} is not $\lambda_g/4$. The impedance matching and bandwidth of Port 2 can be improved by adding a new shorting wall at $\lambda_g/4$ distance, $d_{p2} = 8.8$ mm, from Port 2, which does not affect the performance of Port 1. The grating polarizer, a grid of wires, is positioned between the two ports, and it is transparent to the y-polarized wave generated by Port 1 and acts as a shorting wall for the x-polarized wave generated by Port 2.

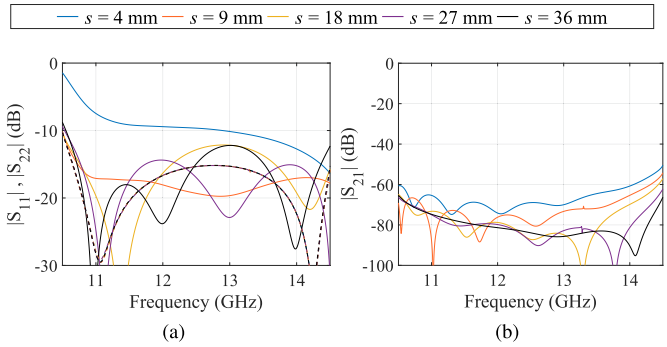

Fig. 2. (a) Reflection coefficients of Port 1 ($|S_{11}|$ —) and Port 2 ($|S_{22}|$ - -) and (b) coupling between the ports w.r.t. s, where $w_a = w_b = 1$ mm and $g = 2.6$ mm of the OMT.

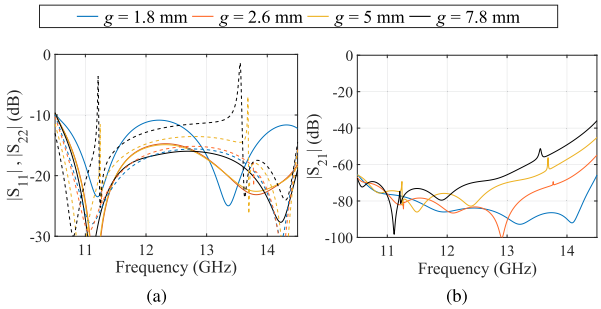

Fig. 3. (a) Reflection coefficients of Port 1 ($|S_{11}|$ —) and Port 2 ($|S_{22}|$ - -) coupling between the ports w.r.t. g when $w_a = w_b = 1$ mm, $s = 27$ mm of the OMT.

The OMT parameters that affect $|S_{11}|$, $|S_{22}|$, and $|S_{21}|$ are: 1) separation between the Port 1 and grating polarizer, s, 2) center-to-center distance between the polarizer wires, g, and 3) cross-sectional dimensions of the polarizer wire w_a and w_b. In this section, the effects of above-mentioned OMT parameters are studied and the simulation model is shown in Fig. 1. The square waveguide is terminated with a waveguide port that supports all the modes.

Fig. 2 shows that $|S_{11}|$ is high when the grating polarizer is placed close to Port 1, $s = 4$ mm $< \lambda/4$. As s increases, $|S_{11}|$ decreases and $|S_{11}|$ reaches its minimum when $s = 9$ mm $\approx \lambda/4$. Though $|S_{11}|$ is minimum at $s \approx \lambda/4$, $|S_{21}|$ can be further decreased by increasing s. The coupling begins to saturate when s is greater than 24 mm. However, when s is larger than $\lambda/4$, $|S_{11}|$ increases and reaches its maximum when $s = 18$ mm $\approx \lambda/2$ and $|S_{11}|$ has the next minimum when $s = 27$ mm $\approx 3\lambda/4$ mm. $|S_{22}|$ is not affected by the positioning of the grating polarizer.

Fig. 3 illustrates the effects of the separation between the grating wall wires or gap g on $|S_{11}|$, $|S_{22}|$, and $|S_{21}|$. When g is 1.8, 2.6, 5, and 7.8 mm, the number of the polarizer wires is 7, 5, 3, and 1, respectively. As the gap increases, the reflection from the grating wall, seen in the decrease of $|S_{11}|$, decreases. With increasing g, the coupling $|S_{21}|$ increases, especially toward the higher frequency. Once the gap in the grating wall increases, the grating wall does not behave as a perfect short for Port 2. The waveguide section between the polarizer and the back wall supports resonances at some frequencies, i.e., at 11.25 and

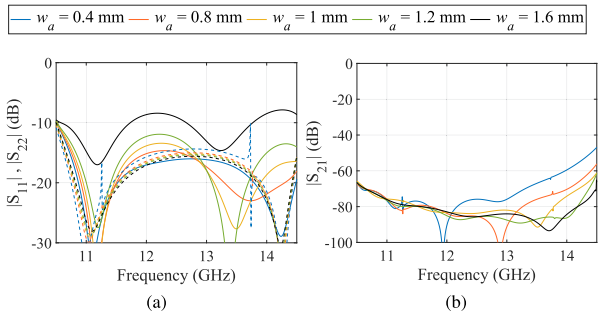

Fig. 4. (a) Reflection coefficients of Port 1 ($|S_{11}|$ —) and Port 2 ($|S_{22}|$ - -) and (b) coupling between the ports w.r.t. w_a when $w_b = 1$ mm, $g = 2.6$ mm, and $s = 27$ mm of the OMT.

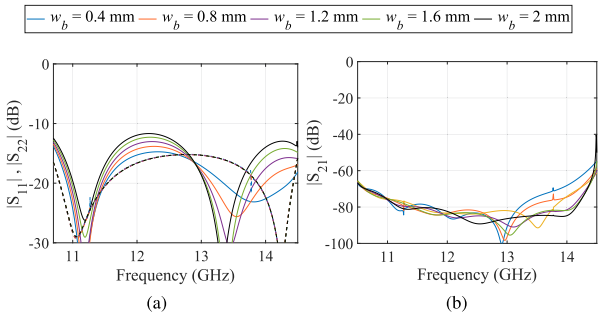

Fig. 5. (a) Reflection coefficients of Port 1 ($|S_{11}|$ —) and Port 2 ($|S_{22}|$ - -) and (b) coupling between the ports w.r.t. w_b when $s = 27$ mm, $w_a = 1$ mm and $g = 2.6$ mm of the OMT.

13.5 GHz. Due to the imperfect isolation of the polarizer, this resonating cavity couples weakly to Port 2.

Fig. 4 illustrates the effects of the grating wall thickness w_a on $|S_{11}|$, $|S_{22}|$, and $|S_{21}|$. For the fixed gap of 2.6 mm, the smaller w_a enables lower $|S_{11}|$, however it increases $|S_{21}|$. With the smaller w_a, the resonances at 11.25 and 13.75 GHz appear as previously with the sparse grating wall. As w_a increases, $|S_{11}|$ increases, $|S_{22}|$ slightly decreases, and $|S_{21}|$ also decreases, especially at higher frequency. $|S_{11}|$ increases due to increase in the thickness of the grating wall. The effects of the wire width w_b and wire thickness w_a are similar. The growing w_b increases $|S_{11}|$, does not affect $|S_{22}|$, and improves $|S_{21}|$ at higher frequency, see Fig. 5.

In summary, the parametric study illustrates that the design of the OMT is a tradeoff between reflection coefficients, isolation, and the size, i.e., separation distance between the feed ports. The lower coupling can be achieved with smaller g, larger w_a, and larger w_b, however, at a cost of an increased reflection coefficient of Port 1. Similarly, the coupling can be minimized with larger s, however, at the cost of an increased volume of the OMT. The simulation results also show that the coupling starts to increase after 14 GHz in all cases. The increase is mainly due to presence of the higher order mode as the cutoff frequency of the TE_{11} mode is closer.

III. Dual-Polarized Probe

In this section, the DPP, a combination of an OMT and a radiating element, is presented. A square OEWG is used as

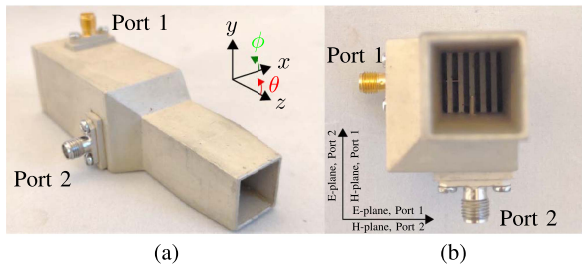

Fig. 6. (a) Perspective and (b) top view of the fabricated DPP.

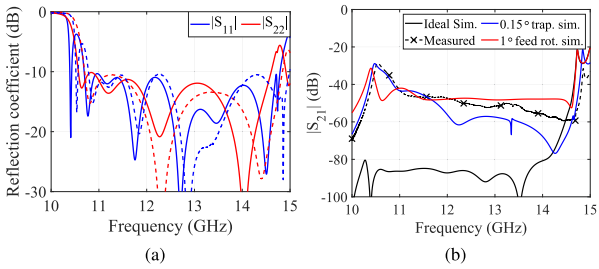

Fig. 7. Simulated (—) and measured (- -) (a) reflection coefficients and (b) coupling between Port 1 and Port 2 of the DPP.

the radiating element as shown in Fig. 6. The cross-sectional dimensions of the OMT and OEWG are the same, i.e., 14.55 mm. The designed OMT parameters s, g, w_a, and w_b are 27, 2.6, 1, and 1.25 mm, respectively. The total length of the DPP, i.e., OMT and OEWG, is 97.5 mm. The radiating aperture of the DPP is chamfered to minimize the multiple reflections between the probe and the AUT. The probe walls are made thicker in two directions to adjust the center-pin lengths of the coaxial connectors inside the waveguide.

The probe is fabricated using the plastic additive manufacturing and then metallized with conductive paint, see photographs in Fig. 6. The prototype is printed using Ultimaker S5 with the layer thickness of 0.06 mm, and the print speed of 30 mm/s is used to achieve the high accuracy. Total print time is approx. 16 h. The conductivity of the applied silver paint is 1.3×10^6 S/m [17]. The skin depth at the lowest frequency, 10 GHz, is 0.5 μm. In order to ensure uniform metallization with thickness greater than the skin depth, three layers of silver paint is applied with the curing time of 8 h. The measured cross-sectional dimensions of the square waveguide are approx. 14.4 and 14.45 mm along x- and y-directions, respectively.

The comparison between the simulated and measured S-parameters of the DPP is shown in Fig. 7. The simulated $|S_{11}|$ and $|S_{22}|$ of the ideal probe, i.e., without manufacturing defects, is below -10 dB between 10.7 and 14.5 GHz. The impedance matching, $|S_{11}|$ and $|S_{22}|$, of the DPP can be further improved by using additional stubs or shaped coaxial feeds at the coaxial-to-waveguide transition [18]. Furthermore, the reflections at the radiating aperture can be minimized with flared horn-like radiating aperture or slots in the radiating wall [19]. However, the above-mentioned changes in the coaxial-to-waveguide transition and the radiating aperture increase the manufacturing challenges and increase the radar cross section of the probe

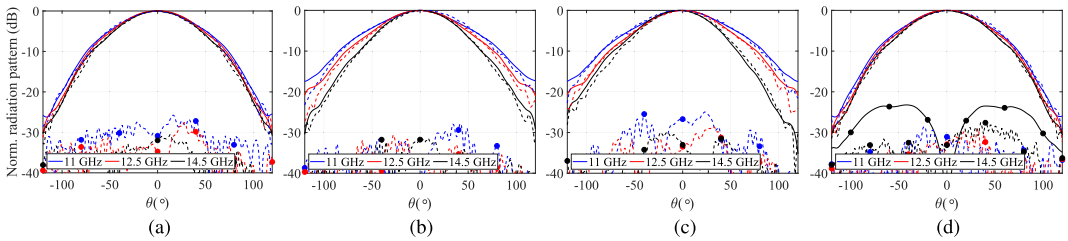

Fig. 8. Comparison of the simulated (—) and measured (- - -) normalized radiation pattern along (a) H-plane and (b) E-plane of Port 1 and (c) E-plane and (d) H-plane of Port 2. Marker (-●-) represents the polarization orthogonal to the main polarization.

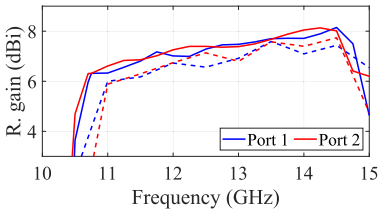

Fig. 9. Simulated (—) and measured (- -) realized gain of the DPP.

antenna. The simulated and measured $|S_{11}|$ and $|S_{22}|$ are in good agreement, except that the measured S-parameters are slightly shifted higher in frequency, by approx. 120 MHz, which is caused by slightly smaller cross-sectional dimensions of the fabricated square waveguide, see Fig. 7(a).

The simulated coupling is below -60 dB in the designed frequencies, whereas the measured one is below -40 dB between 10.9 and 14.8 GHz, as shown in Fig. 7(b). The measured coupling is higher than the simulated mainly due to the manufacturing inaccuracies. The simulated $|S_{21}|$ of the DPP presented in Fig. 7(b) illustrates that the coupling level can raise from below -80 dB, in the ideal case, to approximately -50 dB with potential miniscule inaccuracies such as the coaxial connector being tilted by 1° (red) or the angle between the adjacent wall of the square waveguide is off by 0.15° (blue). It is difficult to be certain of the exact reason and amend it with the current manufacturing process. With the manufacturing inaccuracies, the coupling gets even higher at lower frequencies, i.e., at less than 11 GHz, due to following two factors. First, at lower frequencies the impedance mismatch at the radiating aperture of the waveguide is higher, therefore, the reflections, and thus also the coupling increases. Second, at lower frequencies, the beamwidth of the probe is wider, hence the asymmetry of the outer probe structure starts to affect the radiation and consequently the coupling performance.

The far-field radiation patterns are measured in the anechoic chamber. Fig. 8 shows the measured co- and cross-polar patterns of Port 1 and Port 2 along the principle axes of the DPP. The measured co-polar or the main polarization radiation patterns of the both ports agree well with the simulations. The minor difference at higher θ angles $>90^\circ$ is mainly due to the difference in the size of the absorber used in the simulations and measurements. However, the radiation toward large θ angles is not important, as far it is low, in the anticipated planar NF measurement application. The simulated (and measured) half-power beamwidths along the E-plane are 80° (85°), 74° (76°), and 68° (66°) at 11, 12.5, and 14.5 GHz, respectively. The simulation studies show that the polarization properties of the DPP are similar to those of the square waveguide. The measured and simulated cross-polar radiation of both ports are less than -25 dB and -45 dB, respectively, along the major axes. The higher cross-polar radiation is caused by inaccuracies in the manufacturing and less effective absorbers used in the measurements. The main beam direction of both the simulation and measured patterns are symmetric and toward the boresight direction except at 14.5 GHz of Port 2, see Fig. 8(c). As mentioned in Section II, at frequencies closer to 14.6 GHz the higher order mode start to affect the propagation of the field inside the waveguide, which affects the direction of the main beam and the level of cross-polarization radiation as shown in Fig. 8(d). The measurement results show that DPP can have higher coupling close to the cutoff frequency of the TE_{10} mode. In addition, the main beam direction changes and the cross-polarization radiation increases closer to the cutoff frequency of the higher order mode TE_{11}. Therefore, in practice the operation bandwidth is limited to 11–14.25 GHz instead of the intended bandwidth of 10.7–14.5 GHz.

Fig. 9 shows the comparison between the simulated and measured realized gain of both the ports. Between 10.7 and 14.5 GHz, the simulated realized gain varies from 6 to 8.1 dBi. The measured gain is at most 0.7 dB lower than the simulated. The slightly lower measured gain might be due to lower conductivity of the silver paint. Simulation study shows that the grating polarizer marginally increases the insertion loss of Port 1 and Port 2 by 0.25 and 0.1 dB, respectively, compared to a traditional square waveguide.

IV. Conclusion

In this letter, the DPP is designed, fabricated, and characterized to operate at Ku-band frequency. The proposed design is simple and has small form-factor compared to the previous solutions. The work also demonstrates that the probe can be fabricated in-house with commonly available 3-D printer and conductive paint. Ideally, the operation bandwidth of the DPP with $|S_{11}|, |S_{22}| < -10$ dB and $|S_{21}| < -60$ dB can be achieved over the bandwidth of approx. 30%. The measurement results have demonstrated that the fabricated probe operated well, $|S_{11}|, |S_{22}| < -10$ dB and $|S_{21}| < -40$ dB, between 11 and 14.25 GHz, i.e., the bandwidth is approx. 26%.

Acknowledgment

The authors would like to thank Matti Kuosmanen for advice in using conductive paint.

REFERENCES

[1] A. C. Newell and M. L. Crawford, "Planar near-field measurements on high performance array antennas," *Nat. Bur. Stand.*, NBSIR 74-380, Jul. 1974.

[2] A. C. Newell, "Error analysis techniques for planar near-field measurements," *IEEE Trans. Antennas Propag.*, vol. 36, no. 6, pp. 754–768, Jun. 1988.

[3] A. Yaghjian, "Approximate formulas for the far field and gain of open-ended rectangular waveguide," *IEEE Trans. Antennas Propag.*, vol. AP-32, no. 4, pp. 378–384, Apr. 1984.

[4] S. K. Karki, J. Ala-Laurinaho, V. Viikari, A. Alanne, P. Moseley, and M. Simeoni, "Positioning of orthogonally-polarized waveguide probes for near-field antenna measurement," in *Proc. 15th Eur. Conf. Antennas Propag.*, 2021, pp. 1–5.

[5] L. J. Foged, A. Giacomini, and R. Morbidini, "Dual polarized probe for wideband planar near field measurement applications," in *Proc. 5th Eur. Conf. Antennas Propag.*, 2011, pp. 3402–3406.

[6] S. Skinner and G. James, "Wide-band orthomode transducers," *IEEE Trans. Microw. Theory Techn.*, vol. 39, no. 2, pp. 294–300, Feb. 1991.

[7] R. M. Moreno, J. Ala-Laurinaho, and V. Viikari, "Rod waveguides as future 5G antennas for mobile devices," in *Proc. 48th Eur. Microw. Conf.*, 2018, pp. 1081–1084.

[8] Z. Shen and C. Feng, "A new dual-polarized broadband horn antenna," *IEEE Antennas Wireless Propag. Lett.*, vol. 4, pp. 270–273, 2005.

[9] L. J. Foged and A. Giacomini, "Wide band dual polarized probes for near and farfield measurement systems," in *Proc. IEEE Antennas Propag. Soc. Int. Symp.*, 2008, pp. 1–4.

[10] A. Navarrini and R. Plambeck, "A turnstile junction waveguide orthomode transducer," *IEEE Trans. Microw. Theory Techn.*, vol. 54, no. 1, pp. 272–277, Jan. 2006.

[11] G. Pisano et al., "A broadband WR10 turnstile junction orthomode transducer," *IEEE Microw. Wireless Compon. Lett.*, vol. 17, no. 4, pp. 286–288, Apr. 2007.

[12] A. Giacomini, L. J. Foged, E. Szpindor, W. Zhang, and P. O. Iversen, "High performance dual polarized near-field probe at V-band provides increased performances for millimeter wave spherical near-field measurements," in *Proc. Antenna Meas. Techn. Assoc. Symp.*, 2017, pp. 1–6.

[13] P. I. Muntianu and O. Breinbjerg, "A 60 GHz first-order dual-port probe for spherical near-field antenna measurements," *IEEE Antennas Wireless Propag. Lett.*, vol. 19, no. 9, pp. 1467–1470, Sep. 2020.

[14] M. Chung, D. Je, and S.-R. Kim, "A broadband W-band orthomode transducer for KVN polarization observations," *J. Astron. Space Sci.*, vol. 30, pp. 345–353, 2013.

[15] T.-L. Zhang, Z.-H. Yan, L. Chen, and F.-F. Fan, "Design of broadband orthomode transducer based on double ridged waveguide," in *Proc. Int. Conf. Microw. Millimeter Wave Technol.*, 2010, pp. 765–768.

[16] A. Williamson, "Coaxially fed hollow probe in a rectangular waveguide," *IEE Proc. H. (Microw., Antennas Propag.)*, vol. 132, no. 5, pp. 273–285, 1985.

[17] MG Chemicals, "842WB Liquid," 842WB Liquid Datasheet, Surrey, BC, Canada, Accessed: Mar. 2022. [Online]. Available: https://www.mgchemicals.com/downloads/tds/tds-842wb-l.pdf

[18] A. J. Lozano-Guerrero, F. J. Clemente-Fernandez, J. Monzo-Cabrera, J. L. Pedreno-Molina, and A. Diaz-Morcillo, "Precise evaluation of coaxial to waveguide transitions by means of inverse techniques," *IEEE Trans. Microw. Theory Techn.*, vol. 58, no. 1, pp. 229–235, Jan. 2010.

[19] S. K. Karki, J. Ala-Laurinaho, and V. Viikari, "Low-profile scanloss-reduced integrated metal-lens antenna," *IEEE Trans. Antennas Propag.*, vol. 70, no. 2, pp. 876–887, Feb. 2022.